

# High-frequency bistatic scattering experiments using proud and buried targets

Ph. Blondel<sup>1</sup>, P.F. Dobbins<sup>1</sup>, N. Jayasundere<sup>1</sup>, M. Cosci<sup>1,2</sup>

<sup>1</sup> Department of Physics, University of Bath, Bath BA2 7AY, UK

<sup>2</sup> Visiting student from University of Pisa, Pisa, Italy

## Abstract

*Emergent technologies such as Autonomous Underwater Vehicles and bistatic sonars offer immense leverage to the modern applications of underwater acoustics. However, high-frequency scattering processes need to be better understood, especially in multiple-target environments (e.g. dumpsites or highly cluttered seabeds). Using our facilities at the University of Bath, we have conducted scaled experiments in a large water tank containing several sediment trays representative of continental margin seabeds. This work is part of the SITAR project, funded by the European Commission and investigating the risks caused by buried toxic waste. We therefore used scaled targets comparable to the toxic waste containers found in many dumpsites at sea (fluid-filled cylinders, empty cylinders, spheres, boxes, etc.). Multiple targets (up to 4) were imaged with a narrow acoustic beam at different incidence angles. The receiving hydrophones were positioned to correspond to a vertical linear array some distance away from the targets. This set-up is a scaled-down version of the SITAR sea trials performed in September/October 2003 in the Stockholm Archipelago, except that it offers a totally controlled laboratory environment. Systematic and thorough bistatic measurements were carried out as a function of both scattering angle and bistatic angle. The targets were arranged in different ways, and the differences and similarities between the results associated to these configurations are presented. Advanced deconvolution methods and search routines have been used to reconstruct acoustic scattering inside and outside the different objects. After discussing the influence of the interior of the targets, their distribution, and the influence of the enclosing seabed, we present the possible implications for multiple-aspect surveys. This is followed with presentations of the early results from the processing of the tank and sea trials data, and a discussion of their significance.*

## 1. Rationale

The last decades have shown acoustic instruments were paramount in mapping the seabed and detecting structures at its surface or in its immediate sub-surface. The spatial resolutions now available range from a hundred metres down to a few centimetres, spanning four orders of magnitude and a whole range of physical, geological and anthropological processes (e.g. Blondel and Murton, 1997; Lurton, 2002). Small or man-made objects located on or below the seafloor are however still rather difficult to find. Important and on-going research efforts are devoted to their acoustic detection and recognition (e.g. Pace et al., 1997). Multiple-target environments (e.g. dumpsites, or cluttered zones) are particularly difficult to investigate, and often only the location and extent of the largest targets can be determined. Further details, such as their physical state (integrity/corrosion) or the numbers/positions of smaller targets, are still generally inaccessible.

Simulations and practical use of high-frequency acoustic scattering show the potential offered by bistatic geometries to detect small targets on/in the seabed, and sometimes to identify some of their smaller details or characteristics (e.g. Blondel et al., 2002, Canepa et al., 2002; Burnett and Zampolli, 2004). The emergence of new technologies, such as Autonomous Underwater Vehicles, adds to the growing interest for bistatic sonars. Using our facilities at the University of Bath, we have therefore decided to investigate experimentally the bistatic scattering from proud and buried objects, and how it could be used to reconstruct their characteristics.

In the following Section, we will introduce the experimental set-up, and justify the different choices made. This Section will present scattering results for bare seabeds, followed with scattering from different types of scaled targets, proud or buried at varying levels, and with varying orientations. It will end with a presentation of results for multiple-target configurations, showing the relative influences of the incidence, scattering and bistatic angles.

The next Section will show how the acoustic waveforms collected at different ensonifying geometries can be used to, first, detect the presence of target(s), second to locate it and even reconstruct its acoustic characteristics. The first task is based on an adaptive implementation of the non-recursive Wiener filters traditionally used in seismic processing, while the localisation of the target(s) uses multidimensional search routines based on a downhill simplex algorithm. Typical processing results from the tank experiments are presented, showing the good agreement between the actual and inferred locations of the targets (as well as their characteristics).

The concluding Section summarises these techniques and their application to experimental tank data. This leads to the SITAR sea trials, performed in September/October 2003 in the Stockholm Archipelago. Their preliminary results will be presented in relation to the tank experiments, including a discussion of similarities (and differences) between both modes of operation, and what can be learnt in both cases.

## **2. Bistatic Scattering Experiments**

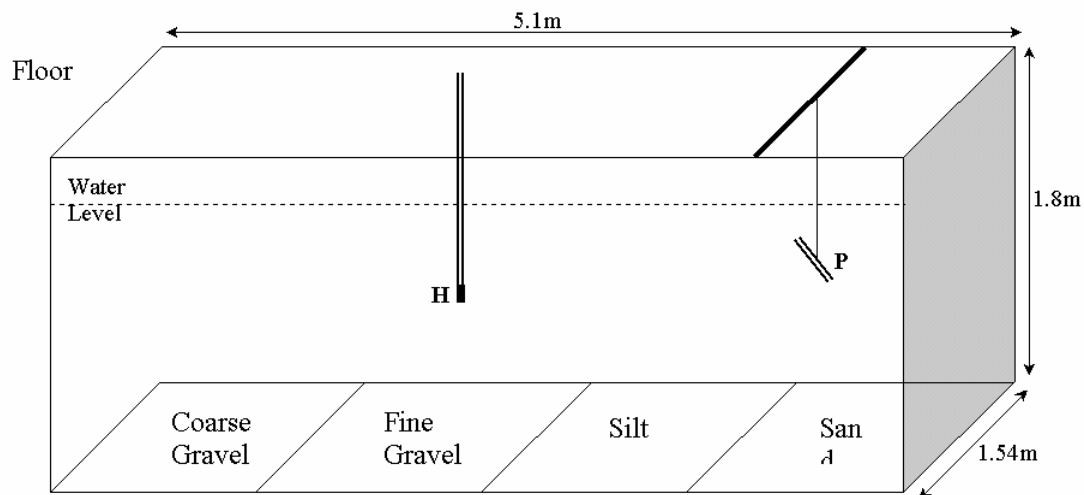
### *2.1. Scaled Tank Experiments*

The incentive for this work was the investigation of risks caused by buried toxic waste, as part of the SITAR project (funded by the European Commission) and the preparation of sea trials in the Stockholm Archipelago in 2003. Acoustic studies of the seafloor make an ever-increasing use of high frequencies (10 kHz and beyond). To make sense and quantitatively assess the acoustic measurements thus obtained, several models of bistatic scattering have been developed over the years. They include refinements to the Kirchhoff approximation (e.g. Thorsos, 1988a; Wirgin, 1989; Ivanova and Broschat, 1993), exact integral solutions (e.g. Schenk, 1986; Thorsos, 1988b; Kirkup, 1998), Small-Slope Approximation (Voronovich, 1985; Thorsos and Broschat, 1995; Broschat and Thorsos, 1997), waveguide propagation models (e.g. Schmidt and Glattetre, 1985; Schmidt and Kuperman, 1995), composite-roughness models (e.g. Kur'yanov, 1963; McDaniel and Gorman, 1983) and hybrid models (Jackson, 1993; Williams and Jackson, 1996; Pouliquen et al., 1999). But the comparison of these models with actual data is hampered by the lack of actual measurements, especially at higher frequencies (above 100 kHz). It is therefore necessary to perform experiments, to understand the optimal imaging geometries and to refine the sonar signal processing techniques.

Very few sea experiments have been performed so far, most of which have taken place in selected shallow-water sites on the continental shelf (e.g. Williams and Jackson, 1998; Blondel et al., 2001; Canepa et al., 2002). These experiments are fraught with difficulties, not all of which could be expected. One can for example list unexpected variations in the seabed, unexpected variations in the water column, or unexpected effects (e.g. ship hull reflections, target burial during the time of the experiment). Because of their complexity, the results of most experiments are still

being fully analysed. They have however revealed the complex interactions between targets and their environments.

Conversely, laboratory experiments are easier to perform, at least in theory: the environmental variations can be controlled; the target emplacement is known with very high accuracy; the target-background interactions can be directly measured and the experimental uncertainties (e.g. transducer positions) are tightly controlled. Using our facilities at the University of Bath, we have conducted scaled experiments in a large water tank containing several sediment trays representative of continental margin seabeds (Figure 1). We used scaled targets comparable to the toxic waste containers found in many dumpsites at sea. Multiple targets (up to 4) were imaged with a narrow acoustic beam at different incidence angles. The receiving hydrophones were positioned to correspond to a vertical linear array some distance away from the targets. This set-up is a scaled-down version of the SITAR sea trials performed in September/October 2003 in the Stockholm Archipelago, in a totally stable and controlled setting. The influence of the environmental and experimental uncertainties had already been modelled (and measured) by Blondel et al. (2001, 2002).



P – Projector; H – Hydrophone.

Figure 1. The University of Bath underground tank facilities. The walls are made of concrete, and the top of the tank is at floor level. The sediments in the trays are 14 cm deep in average. The water level can be varied and was fixed at 1.475 m in this case. Both the acoustic projector and the hydrophone(s) can be positioned anywhere in the tank. The targets are oriented relative to the  $X$  axis (lengthwise), the  $Y$  axis (along the 1.54-m width of the tank), or the  $Z$  axis (vertically). They were also placed diagonally ( $XY$  orientation).

A scaling factor of approximately 10:1 was used in the design of the experiments. The targets were designed to match the numerical models used during the SITAR project (Skogqvist and Karasalo, 2003) and the types of targets likely to be encountered at the trials site. They are listed in Table 1. Target  $T_1$ , for example, is an approximation of a scaled oil drum, whose standard dimensions are 58 cm in diameter, and 88.5 cm in height. Target  $T_5$  is used for comparison with the numerical simulations of Skogqvist and Karasalo (2003). The SITAR sea trials also showed the presence of a large, metal box. A scaled-down version (target  $T_6$ ) was therefore manufactured, and used in the last series of tank experiments. All 6 targets were used, placed proud, half-buried or flush buried, at different orientations respective to the ensonifying direction, alone or in groups.

T <sub>1</sub>	Sealed Aluminium tin, fluid-filled, 6.7cm(D) x 10cm(L)
T <sub>2</sub>	Air-filled stainless steel cylinder, 5.8cm(D) x 10.4cm(L), sidewall thickness 3mm, end cap thickness 2mm
T <sub>3</sub>	Solid aluminium cylinder, 5.1cm(D) x 8.1cm(L)
T <sub>4</sub>	Solid steel cylinder, 7cm(D) x 8cm(L)
T <sub>5</sub>	Solid brass ring, 10.5cm(D) x 7.5cm(L), wall thickness 7.5mm
T <sub>6</sub>	Air-filled stainless steel box, 10cm x 5cm x 5cm, Wall thickness 2-3mm

Table 1. Dimensions of the scaled targets used in the tank experiments: diameters (D), lengths (L) and other characteristics influencing their acoustic scattering properties.

The four sediment trays at the bottom of the tank are 30 cm deep, and uniformly filled with sediments typical from the European continental margins. The depth of sediment varies slightly from tray to tray. Those used in this study are filled with silt (50  $\mu\text{m}$  mean grain size) and gravel (5 mm mean grain size). The former are a scaled-down version of the soft muddy sediments, with a minute content of gas, expected at the sea trials site (as confirmed later). Karasalo and Skogqvist (2004) used results from previous inversions at nearby sites to obtain tentative values of 1.047 for the sound speed ratio and 1.1 for the density of the sediments, quite close to the values for the silt tray (1.024 and 1.204 respectively). Only the results for the silt tray are presented in this article. The sediment depth inside the silt tray is ca. 14 cm (giving a theoretical attenuation of 184 dB/m at 238 kHz).

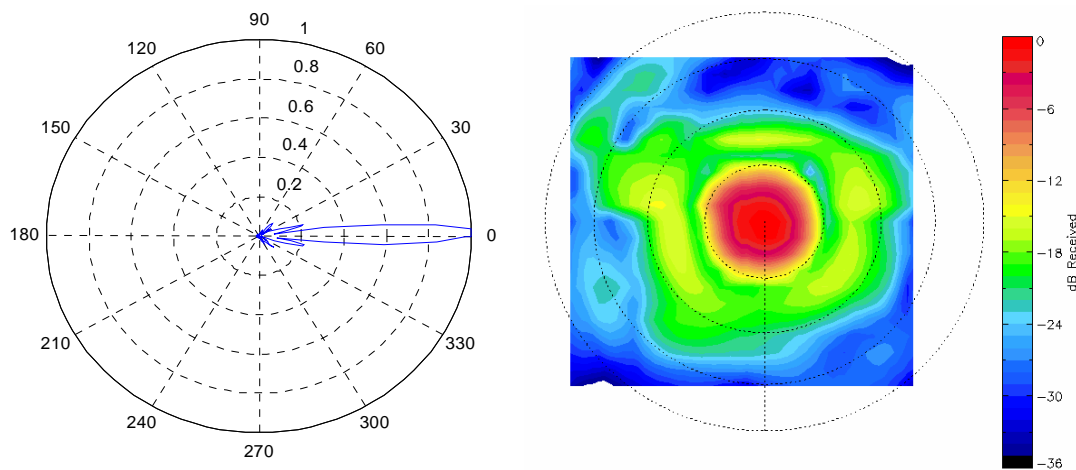


Figure 2. Calibration of the acoustic projector was performed in 2-D (left, in the XY plane) and in 3-D (right, in the XZ plane, with scaling circles every 10°). Note the narrow beamwidth (10°), the small sidelobes, and the asymmetry for the angles further away from the axis of the transducer.

The experiment was arranged in the water tank (5 m x 1.54 m x 1.8 m) according to the setup shown in Figure 1. The height of the water column was 1.475m. The acoustic projector is a damped piezoelectric transducer resonant at 238 kHz, excited with a single sinusoid at 238 kHz with 20 V peak-to-peak amplitude (although other signals, e.g. chirps, were also used later). It has a narrow beamwidth (about 10°), measured in 2-D and in 3-D (Blondel et al., 2001; Jayasundere et al., 2004). The 3-D calibration shows non-symmetrical variations for the angles further away from the axis of the transducer (Figure 2); this needs to be remembered when analysing

scattering from the larger angles. Measurements of the direct signal showed 2 small secondary impulses (respectively 4 and 10 times lower in amplitude), which should also be borne in mind when interpreting the scattered fields. The acoustic projector is mounted on a gantry supported across the tank (Figure 3), allowing its tilt to be set to any desired angle. The transducer was positioned 0.5 m away from the target(s).

The receiver is an omnidirectional hydrophone Brüel & Kjaer (B&K) 8103, fixed to the end of a 9-mm diameter stainless steel tube. The tube is mounted on a translation/rotation stage, positioned in line with the projector and the target (Figure 3, top). Two types of experiments were performed: line scans and rotation scans. In line scans, the hydrophone was positioned 0.5 m above the seabed, and remotely translated via a PC with a step size of 1 cm, usually starting 1.1 m away from the target, and finishing 15 cm from the target (Figure 3, bottom). In rotation scans, the tube containing the hydrophone was at a fixed distance of 0.5 m from the main target (Figure 3, top), and remotely rotated via a PC, sampling the scattered acoustic field as a function of bistatic angles between  $140^\circ$  and  $220^\circ$  ( $180^\circ$  corresponding to in-plane scattering), with a  $2.5^\circ$  step size. The field was sampled as a function of the scattering angle by manually adjusting the height of the hydrophone over the seabed from 1.375 m to 0.15 m with a step size of 2.5 cm.

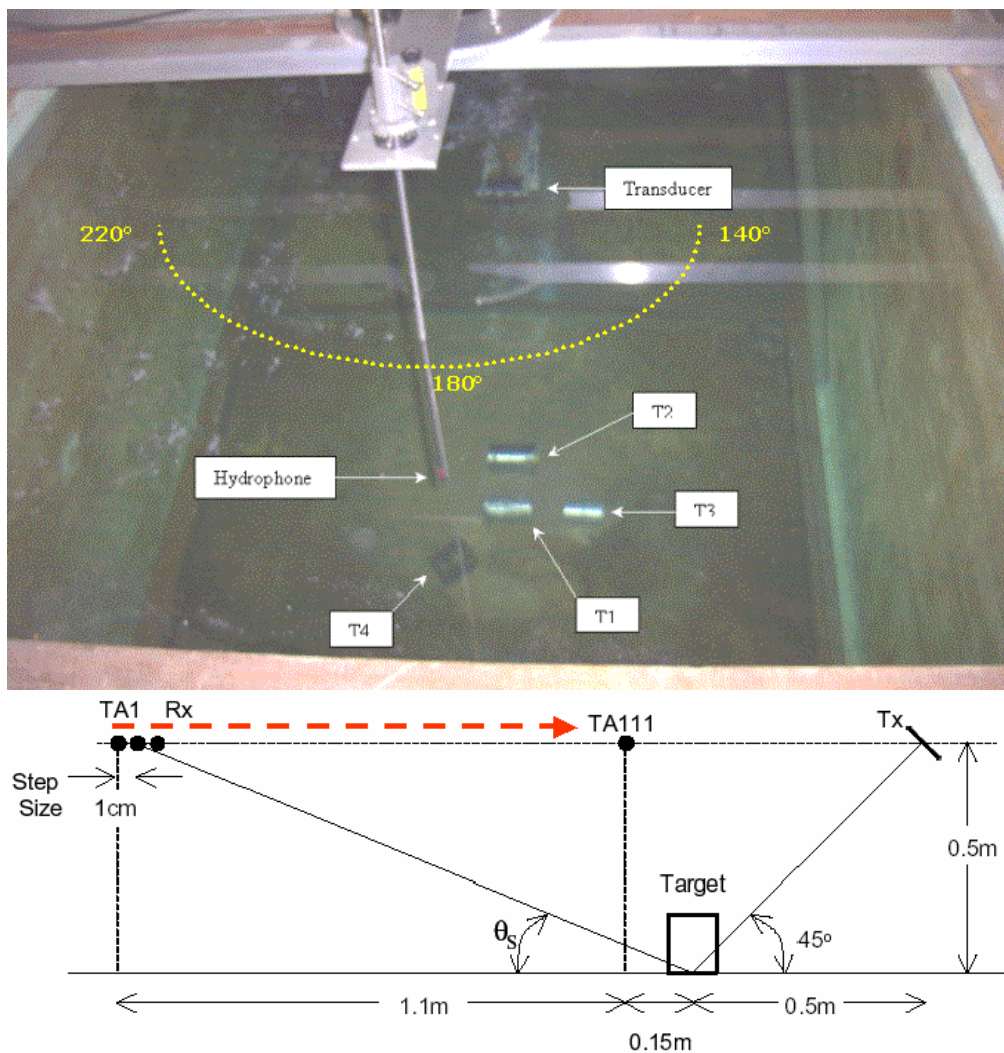


Figure 3. Top: details of a typical rotation scan, for bistatic angles from  $140^\circ$  to  $220^\circ$ . The hydrophone is mounted at the bottom of the stainless steel tube, and measurements at

different scattering angles are obtained by vertically moving the tube. Note the positions of targets  $T_1$ - $T_4$  at the surface of the silt tray. Bottom: diagram of a typical line scan. The hydrophone ( $R_x$ ) starts at position  $TAI$  and scans with 1-cm steps to position  $TAIII$ , giving a range of scattering angles  $\theta_s$ . The transmitter ( $T_x$ ) is tilted at  $45^\circ$  in this case.

These two types of scans correspond to the typical investigation strategies when using ROVs at sea, either "flying lines" over a region or circling objects of interest. They also offer a broader sample of possible bistatic and scattering angles, despite the limitations brought by the finite size of the tank. The total range of configurations sampled is presented in Table 2. The acoustic field was also measured for the bare seabed, before placing the targets and after removing them (to assess any disturbance).

<b>Line scans: incidence angle <math>45^\circ</math> – scattering angles <math>15^\circ</math>-<math>75^\circ</math> (variable according to configuration)</b>			
<i>Target</i>	<i>Configuration</i>	<i>Bistatic angles</i>	<i>Axis orientation</i>
Bare seabed	N/A	$160^\circ, 170^\circ, 180^\circ, 190^\circ, 200^\circ$	
$T_1$	Proud	$160^\circ, 170^\circ, 180^\circ, 190^\circ, 200^\circ$	X, XY, Y and Z
	Half-buried	$160^\circ, 170^\circ, 180^\circ, 190^\circ, 200^\circ$	X and Z
	Flush-buried	$160^\circ, 170^\circ, 180^\circ, 190^\circ, 200^\circ$	Z
$T_2$	Proud	$160^\circ, 170^\circ, 180^\circ, 190^\circ, 200^\circ$	X, XY, Y and Z
	Half-buried	$160^\circ, 170^\circ, 180^\circ, 190^\circ, 200^\circ$	X and Z
	Flush-buried	$160^\circ, 170^\circ, 180^\circ, 190^\circ, 200^\circ$	X and Z
$T_3$	Proud	$160^\circ, 170^\circ, 180^\circ, 190^\circ, 200^\circ$	X, XY, Y and Z
	Half-buried	$160^\circ, 170^\circ, 180^\circ, 190^\circ, 200^\circ$	Z
	Flush-buried	$160^\circ, 170^\circ, 180^\circ, 190^\circ, 200^\circ$	Z
$T_4$	Proud	$160^\circ, 170^\circ, 180^\circ, 190^\circ, 200^\circ$	X, XY, Y and Z
$T_5$	Proud	$160^\circ, 170^\circ, 180^\circ, 190^\circ, 200^\circ$	Z
	Half-buried	$160^\circ, 170^\circ, 180^\circ, 190^\circ, 200^\circ$	Z
	Flush-buried	$160^\circ, 170^\circ, 180^\circ, 190^\circ, 200^\circ$	Z
<b>Line Scans: incidence angle <math>30^\circ</math> – scattering angles <math>15^\circ</math>-<math>75^\circ</math> (variable according to configuration)</b>			
<i>Target</i>	<i>Configuration</i>	<i>Bistatic angle</i>	<i>Axis orientation</i>
Bare seabed	N/A	$180^\circ$	
$T_1$	Proud	$180^\circ$	X and Z
$T_2$	Proud	$180^\circ$	X and Z
$T_3$	Proud	$180^\circ$	Z
<b>Rotation Scans: incidence angle <math>45^\circ</math> – scattering angles <math>14^\circ</math>-<math>70^\circ</math></b>			
<i>Target</i>	<i>Configuration</i>	<i>Bistatic angles</i>	<i>Axis orientation</i>
$T_1$	Proud	$140^\circ$ - $220^\circ$ ( $2.5^\circ$ )	X and Y
$T_2$	Proud	$140^\circ$ - $220^\circ$ ( $2.5^\circ$ )	X
$T_2$	Flush-buried	$140^\circ$ - $220^\circ$ ( $2.5^\circ$ )	X
$T_1+T_2$	Proud	$140^\circ$ - $220^\circ$ ( $2.5^\circ$ )	Y, 11cm apart
$T_1+T_2+T_3$	Proud	$140^\circ$ - $220^\circ$ ( $2.5^\circ$ )	Y, 5 cm from $T_2$ in Y direction
$T_1+T_2+T_3+T_4$	Proud	$140^\circ$ - $220^\circ$ ( $2.5^\circ$ )	Y, 11 cm apart except $T_3$ , which is 5 cm from $T_2$ in Y direction

Table 2. Range of bistatic scattering configurations sampled during this study (silt tray only). The orientation of the main axis of the target is by reference to the horizontal plane (X-Y) and the vertical direction (Z). XY orientations correspond to a target placed diagonally to the main direction of the ensonifying beam.

The output signal from the hydrophone is input to a Brookdeal 9452 precision A.C. amplifier with its gain set to 70 dB, and with the low-pass filter cut-off set to 1 MHz. The amplified output is in turn input to a Krohn-Hite 3202 filter, set to high-pass with a cut-off at 200 kHz. The output of the filter is finally connected to a LeCroy LT-264

digital oscilloscope. The received signals are averaged over 1650 waveforms and further band-pass filtered to reduce the noise level. Post-processing included the deconvolution of each acquired waveform with a replica of the incident signal. The complex envelope was computed with a Hilbert transform. The direct signal was then zero-banded before analysis, removing the redundant information of the direct signal from the projector to the hydrophone. For the analysis as a function of scattering angle, the waveforms were time-shifted, so that the scattered signals arrive with the same time delay at the hydrophones, and weighted, to account for the amplitude fall with distance.

## 2.2. Seabed and Target(s) Scattering

To visualise the experimental measurements, it is easiest to represent the scattered waveforms in the time domain, and look at their relative variations with the scattering angles. The complex amplitude envelope of each waveform is normalised with respect to the maximum amplitude of the data array. "Raw" waveforms already reveal some information, and in particular pronounced differences between the bare seabed and the presence of one or several targets. But they are affected by the original incident signal, usually consisting of several cycles. By deconvolving the scattered waveforms with the projector's signal, the complex envelope improves the overall image resolution. Figure 4 shows the scattering off the bare seabed (left) and the bare seabed with only one target (right). The acoustic scattering from the target ( $T_1$ , in this case), placed vertical and proud, is significant, at scattering angles between  $24^\circ$  and  $65^\circ$ . It comes immediately before the return from the seabed, which should be expected as it stands higher. There are also some contributions from the reflections of signals from the surface of the water and the tank walls, later in time. As explained in Section 2.1, the acoustic field scattered by the bare seabed was sampled before placing the targets, and after removing them, to assess any disturbance. Visual comparison (and/or subtraction) of the normalised amplitude fields before and after would show any significant differences, likely to cause problems for the next target studies (fortunately, this did not happen during this series of experiments using the silt tray).

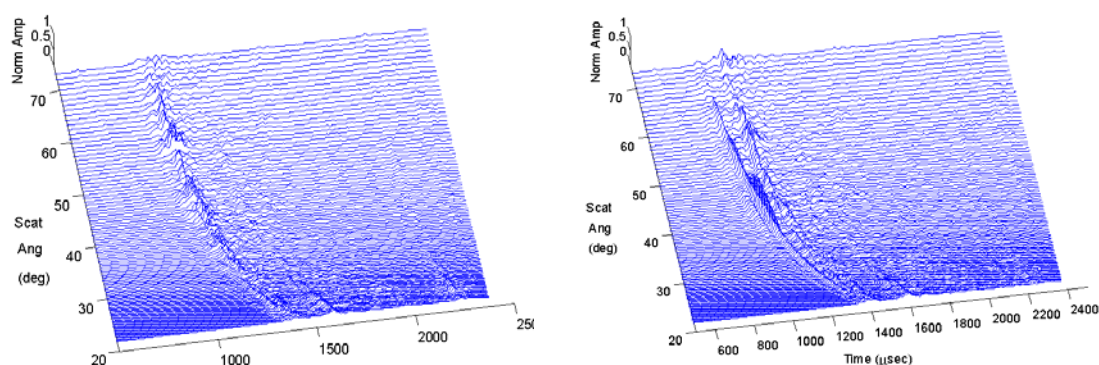


Figure 4. Scattered waveforms for bare silt (left) and with target  $T_1$  proud in the Z direction, i.e. placed vertically on the seabed (right). In this case, the incidence angle is  $45^\circ$  and the bistatic angle is  $180^\circ$  (in-plane scattering). The normalised amplitudes of the scattered waveforms are plotted as a function of time and the scattering angle at which they were measured.

Representing the scattered waveforms as contour maps makes it easier to spot differences. Figure 5(left) shows the scattered field, measured as a function of the scattering angle only for one target, in this case  $T_1$  (fluid-filled cylinder). The bistatic angle still is  $180^\circ$  (in-plane scattering) and the incidence angle is  $45^\circ$  again. The target

was placed horizontally along the  $X$  axis of the tank (Figure 1). The normalised amplitudes are plotted as a contour map, with 20 contours equidistant between 0 (no return) and 1. The image for  $T_1$  is characterized by a single region of high scattering amplitude, increasing in magnitude with the scattering angle. A small region of somewhat higher normalised amplitudes is visible at later times (ca. 470  $\mu\text{s}$ ); it is apparently associated to reflections from perturbed parts of the seabed. This contour map can be readily compared to the case of two targets,  $T_1$  and  $T_2$  (air-filled cylinder). The field scattered from  $T_2$  arrives earlier than that of  $T_1$  (Figure 5, right). The image is characterized by interference patterns of the direct arrivals from  $T_1$  and  $T_2$  and an interacting region between them. These can be linked to the different waves propagating at the surface of the targets, some of which will be reemitted (e.g. Blonigen and Marston, 2002; Tesei et al., 2002). Adding a third target (in this case  $T_3$ , the solid aluminium cylinder) does not alter significantly the overall scattering pattern.

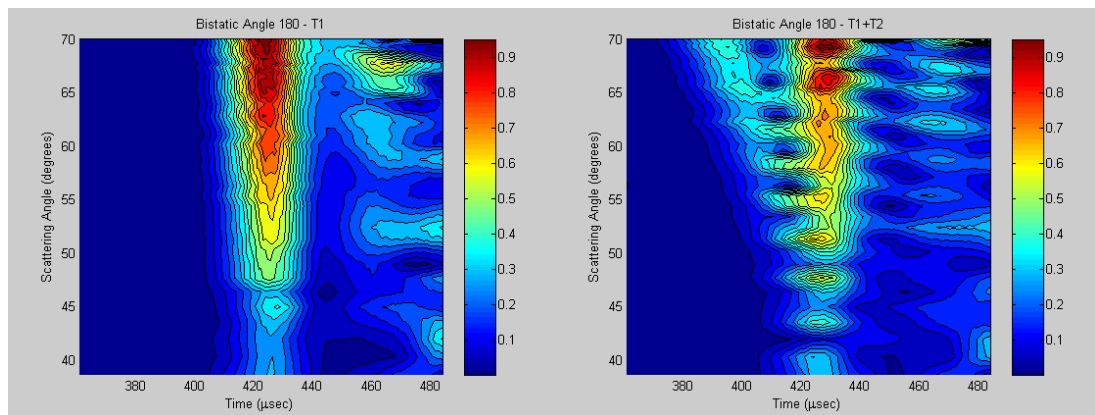


Figure 5: Contour maps of the normalised amplitude as a function of the scattering angle for a bistatic angle of  $180^\circ$ , for target  $T_1$  alone (left) and targets  $T_1+T_2$  (right).

To investigate the contribution of a third target, like  $T_3$ , the bistatic angle needs to change. Figure 6(left) shows the combined scattering of targets  $T_1$  and  $T_2$ , for the same incidence angle of  $45^\circ$  but at a bistatic angle of  $160^\circ$  (i.e.  $20^\circ$  away from in-plane scattering). The images in Figure 6(left) and Figure 5(right) are relatively similar. The relative amplitudes of the peaks corresponding to scattering by  $T_1$  and  $T_2$  are more distinct. This is logical, as with a bistatic angle of  $160^\circ$ , a larger portion of target  $T_2$  is ensonified (cf. Figure 3, top). The same interference patterns between the direct arrivals from  $T_1$  and  $T_2$  are also visible. The high amplitude regions starting at approximately 460  $\mu\text{sec}$  are also due to scattering from irregularities on the seabed. Figure 6(right) now shows the combined scattering of targets  $T_1$ ,  $T_2$  and  $T_3$ , with the same incidence angle of  $45^\circ$  and bistatic angle of  $160^\circ$ . The contribution of target  $T_2$  has greatly reduced, with interference between the scattered signals from  $T_1$  and  $T_3$  dominating the image. This was also expected, as, when moving away from in-plane scattering in this direction, the geometry of the direct path between the acoustic projector and the hydrophone covers more of target  $T_3$ . The effects of the irregularities at the surface of the sediment tray are now more pronounced when observed with a different bistatic angle. This effect confirms simulations and earlier experiments in the same tank (Blondel et al., 2002).

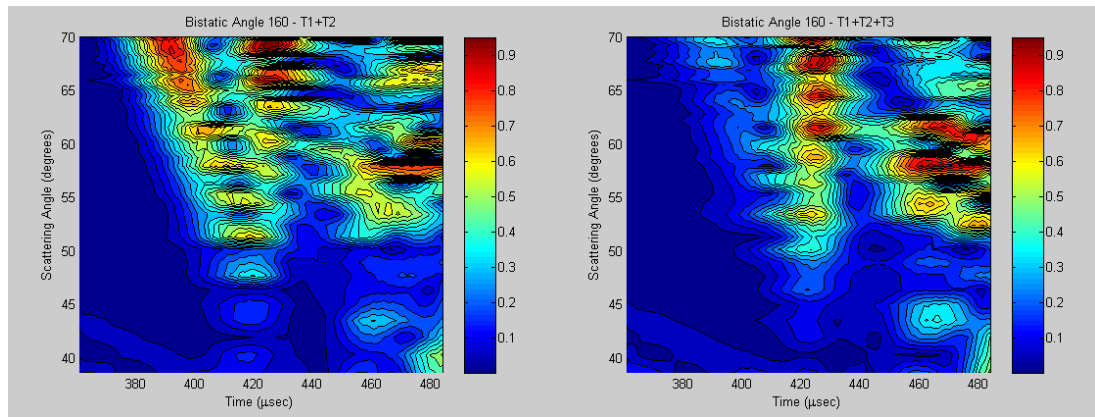


Figure 6: Contour maps of the normalised amplitude as a function of the scattering angle, for a bistatic angle of  $160^\circ$ , for targets  $T_1+T_2$  (left) and targets  $T_1+T_2+T_3$  (right).

The addition of a fourth target (in this case  $T_4$ , the solid steel cylinder) does not induce any significant alterations to the overall scattering pattern of the combination of targets  $\{T_1+T_2+T_3\}$ , at least not when plotting contour maps for scattering angles, and a fixed bistatic angle. Instead, to view the contribution from target  $T_4$ , one needs to generate contour maps of the scattering patterns as functions of the bistatic angle (and time), for fixed scattering angles. Figure 7(left) shows the normalised scattered field amplitude for a fixed scattering angle of  $67.4^\circ$  for  $T_1$ ,  $T_2$  and  $T_3$ . Figure 7(right) shows the same for all four targets:  $T_1$ ,  $T_2$ ,  $T_3$  and  $T_4$ . Their comparison shows that  $T_4$  appears at a bistatic angle of  $205^\circ$  around  $1040 \mu\text{sec}$ , later than any of the other targets ( $T_4$  is placed further away: cf. Figure 3, top). The high amplitude region near  $930 \mu\text{sec}$  is due to  $T_2$ , and the one at  $960 \mu\text{sec}$  is due to the combination of  $T_1$  and  $T_3$ .

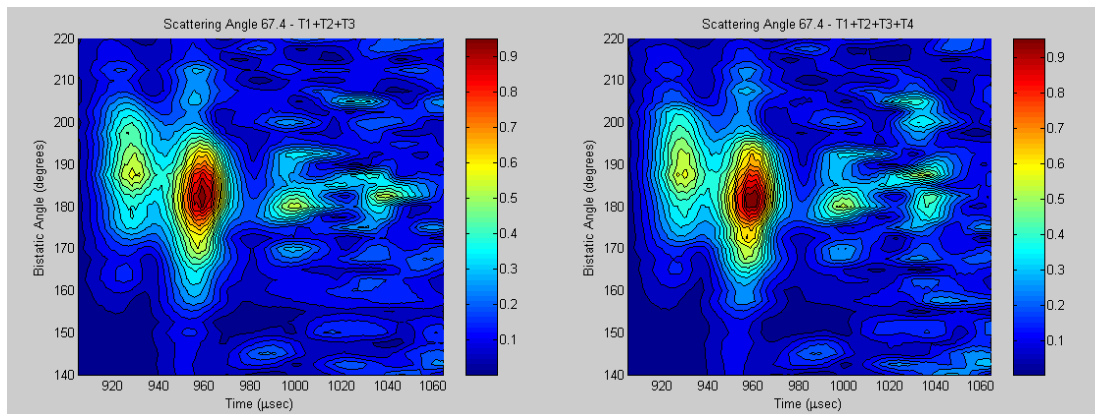


Figure 7: Contour maps of the normalised amplitude, now represented as a function of the bistatic angle, for a scattering angle of  $67.4^\circ$ , for targets  $T_1+T_2+T_3$  (left), and targets  $T_1+T_2+T_3+T_4$  (right).

### 3. Target Detection, Localisation and Acoustic Reconstruction

#### 3.1. Target Detection

The previous Section showed that multiple targets could be visually identified by looking at the waveforms in the time-domain, for different scattering angles, and that careful use of different bistatic angles was often desirable. The examples shown here (Figures 4–7) correspond to a simple input signal, but both the tank experiments and, later, the sea trials, used a variety of transmitted signals (Ricker pulses, chirps, etc.).

Techniques such as cross-correlation with a replica of the transmitted signal work well for chirp signals. For example, a chirp length of 5 ms would yield an effective range resolution of 7.5 m. The main peak of the cross-correlator output would then have a width in the order of 30  $\mu$ s, reducing the spatial resolution to just 4.5 cm. But simple matched filtering is not an effective pulse compression technique for Ricker pulses. Ideally, a deconvolution process is required that will generate a narrow impulse at the effective time-of-arrival for any of the signal types likely to be encountered in a high-frequency active sonar system.

The traditional answer, at least in seismic data processing (e.g. Arya and Aggarwal, 1982; Telford et al., 1990), is to use non-recursive implementations of the Wiener filter:

$$r_t = \sum_{i=0}^{N-1} w_i s_{t-i} \quad (1)$$

where  $r_t$  is the output sample at time  $t$  and  $s_t$  is the input at time  $t$ . The output is a weighted running average over  $N$  samples, with weights  $w_i$  chosen to give a pre-determined impulse at the output when the desired input waveform is present. Generally, a least-squares procedure is used to estimate the set of weights. This filter is effective with clean signals, but where there is noise, when pulses overlap, or if the pulse has been distorted during propagation, the filter fails to generate an impulse of the correct amplitude and at the correct location for every received pulse. The problem is intrinsic because: (1) the autocorrelation function of the input and the cross-correlation between the input and the desired output must be known to compute the correct filter coefficients; (2) when the filter operates in an unknown environment, and the received signal is no longer an exact copy of the transmitted pulse, the information required in (1) may not be available, so the correct filter coefficients cannot be computed.

An estimate of the relative robustness of the process,  $P$ , is given by

$$P = \sum_{i=0}^{N-1} w_i \rho_i \quad (2)$$

where  $\rho$  is the cross-correlation between the desired output pulse and the input signal. Clearly, the greater the similarity between input and output, the more stable the process becomes, but at the price of less effective deconvolution.

To overcome these difficulties, one needs an adaptive implementation, adjusting the coefficients in response to variations in the signals. Bozic (1994) proposed an algorithm based on a variation of Equation (1):

$$\left. \begin{aligned} \hat{r}_t &= \sum_{i=0}^{N-1} w_{i,t} s_{t-i} \\ e_t &= \hat{r}_t - r_t \\ w_{i,t+1} &= w_{i,t} + \mu e_t s_{t-i} \end{aligned} \right\} \quad (3)$$

Here  $\hat{r}_t$  is the desired output impulse and  $r_t$  is the filter output at time  $t$ . At each discrete time step, the updated values of the filter coefficients,  $w_{i,t+1}$  are computed by applying a correction to the previous values  $w_{i,t}$ , derived from an earlier value of the input  $s_{t-i}$  and the difference  $e_t$  between the desired and actual filter outputs, weighted

by a factor  $\mu$ . The process must be initialised with a set of weights derived from an ideal replica of the transmitted signal, as in Equation (1), but it may then be 'trained' on received signals that are known to be single isolated pulses reflected from the bottom or a target of interest, with  $\mu$  set to a value (usually close to unity) that gives reliable convergence to the desired output form. Where such reliable inputs are not present, the adaptation can be 'frozen' by setting  $\mu$  to zero. The decision can be automated by monitoring the cross-correlation between the received signals and the ideal transmission replica. If the peak value falls below a predetermined value the input is not suitable for adaptation, so the process can be frozen.

Figure 8 shows the immediate interest of such a scheme. A fair amount of noise has been added to a typical signal (Figure 8a). Traditional processing, with a non-recursive Wiener filter (Figure 8b), detects some of the high variations (the first positive peak and the largest negative peak only), but keeps the high noise levels. Conversely, the adaptive processing of Equation (3) gives a much cleaner signal (Figure 8c). All significant peaks, positive and negative, are detected, and the noise is considerably reduced.

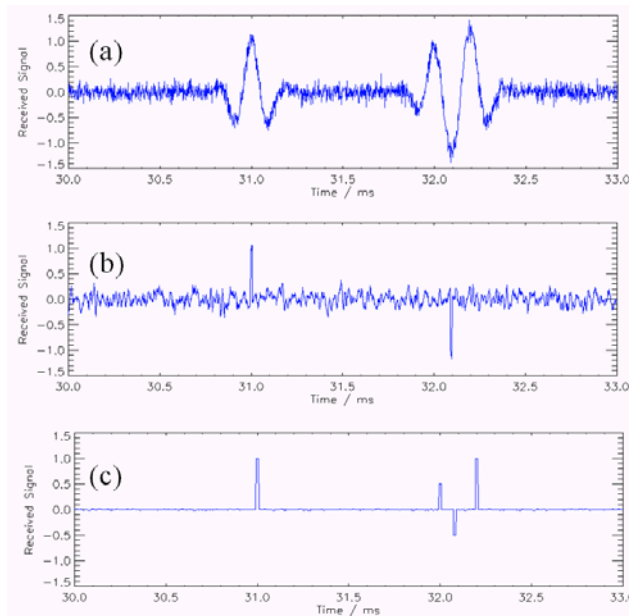


Figure 8. (a) an arbitrary input signal, with high noise, shows the difference between non-recursive Wiener filters (b) and the adaptive implementation optimising the relative weights (c). Note how the noise is considerably reduced in (c), and how the main peaks are correctly detected.

### 3.2. Localisation – Acoustic Reconstruction

Now that a suitable algorithm can detect the peaks related to high scatterers, it can be used to process each waveform (as visible in Figure 4, for example). Each of these waveforms was acquired for a unique set of incidence angle, bistatic angle, and scattering angle. Let us note the respective positions of the transmitter, scatterer and receiver as  $(x_T, y_T, z_T)$ ,  $(x_S, y_S, z_S)$  and  $(x_R, y_R, z_R)$ . In a water column with a constant sound speed  $c$  (a reasonable assumption in the case of the SITAR sea trials, where the distances involved were relatively small, and the absolute truth in the case of the tank experiments), all propagation paths from the transmitter to the scatterer and then on to the receiver (the hydrophone) are straight lines. The total travel time  $T$  is given by

$$T = \frac{1}{c} \left[ \sqrt{(x_S - x_T)^2 + (y_S - y_T)^2 + (z_S - z_T)^2} \dots + \sqrt{(x_R - x_S)^2 + (y_R - y_S)^2 + (z_R - z_S)^2} \right] \quad (4)$$

We know this travel time  $T$  from the deconvolution process (Section 3.1). We know the positions of the source and the receiver. It is therefore possible to solve Equation (3) for the position of the scatterer. This corresponds to the surface of a 3-D ellipsoid. More than one travel path must therefore be considered, to resolve this ambiguity. However, this leads to errors, as the signals received at different hydrophones will have travelled via different scattering points. A method based on a downhill simplex multidimensional search routine (Press et al., 1992) has been developed to minimise this effect. The actual location of the scatterer remains ambiguous, though. This can be remedied by taking the 4 receivers immediately left, right, above and below the receiver considered, and weighing their contributions appropriately (Dobbins et al., 2003). The contours of the error values now lead to a local minimum, close to the actual location. By using the 4 surrounding receivers, the errors tend to cancel, and the ambiguity has been removed.

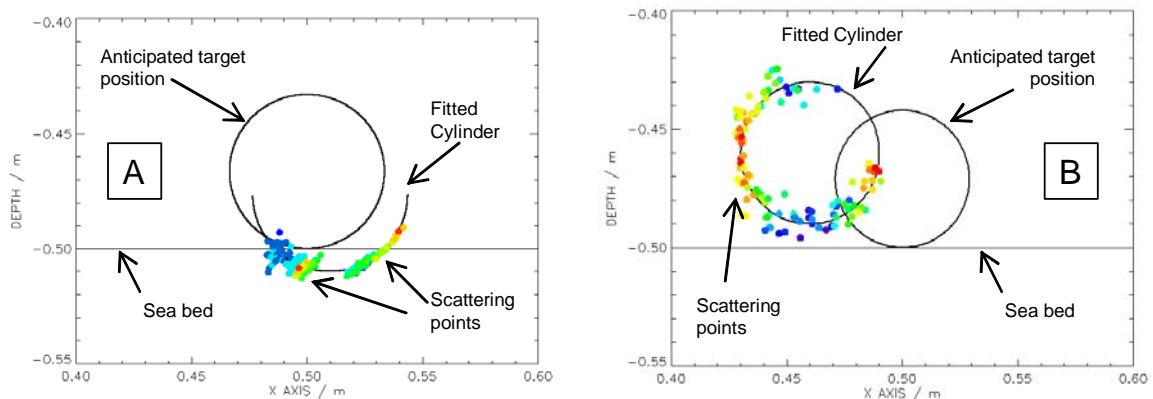


Figure 9. The scattering points, detected and localised using the algorithms presented in the text, are colour-coded according to their respective strengths (from blue, low, to red, high). They are presented next to the anticipated target positions for target  $T_1$  (A) and for target  $T_2$  (B). The offsets from the expected positions are very small, and can be explained by the uncertainty in positioning the targets by hand from the top of the water-filled tank.

Typical results are shown in Figure 9, using data from the tank experiments. The scattering points are localised in 3-D and shown as small circles, shaded to represent their relative scattering strengths (from blue, low, to red, high). Figure 9a shows the reconstruction of target  $T_1$  (fluid-filled aluminium tin, 6.7 cm in diameter). This target was placed horizontally on the sediment surface (and aligned along the  $Y$  axis, here). The scattering points, as detected and located by the algorithm, seem concentrated on the interface between the target and the seabed. The points do not precisely coincide with the expected target position. However, they can be fitted approximately to the lower portion of a cylinder of the same diameter as the target, 1 cm to the right and 1 cm below. The target was positioned manually from the top of the water-filled tank, so an error of around 1 cm in its anticipated position is not surprising, and is small relative to the overall scale of the experiment. It was also found that the target (weighing slightly more than 0.3 kg in air) would not sit totally proud of the seabed, but depressed the surface slightly. Figure 9b shows a similar analysis, for target  $T_2$  (air-filled stainless steel cylinder, 5.8 cm in diameter). There is clearly a more uniform distribution of scattering all around the surface, as might be expected with the greater impedance mismatch in this case. Again, the fitted cylinder is slightly offset from the

expected position (ca. 1 cm in the vertical direction, 4 cm in the horizontal direction), but this result is again satisfactory, especially when remembering the 10:1 scaling factor of these experiments. One can also remark that there are echoes within the same scattered signals, which may provide further information about the target structure (keeping in mind the characteristics of the transducer used, cf. Section 2.1).

Similar results have been obtained with different targets and different target orientations. Overall, they have confirmed the viability of the deconvolution and localisation processes, and they have demonstrated that the scatterer(s) can be located with a precision comparable with the sizes of the targets used in the experiments. Finally, combining the results from runs with hydrophone positions off the  $X$  axis will give us the ability to construct 3-D images of the different targets (Caiti et al., 2003), using the algorithms presented in this Section.

#### **4. Tank Experiments and Sea Trials**

Using the tank facilities at the University of Bath, we have performed a wealth of bistatic scattering measurements, for multiple targets (up to 4 at the same time), on different types of seabeds (only silt was presented here, but similar experiments have been performed on fine gravel too). Single targets are easily identified, by inspection of the different scattering angles at a fixed bistatic angle; they are characterised by a single region of high scattering. An additional target, in line with the source, induces interference, but the two targets are still visible. When adding a third target, one must view the measurements at different bistatic angles. In this case, the interference patterns give a clue to the presence of multiple targets. The effect of adding a fourth target is not very apparent in the images as a function of scattering angle. This may be due to the fourth target being just outside the acoustic beam, and its orientation relative to the other targets. However, its presence is revealed by generating images as a function of bistatic angle at a fixed scattering angle. First analyses of the individual scattering patterns show effects similar to those observed for bare seabeds (Blondel et al., 2001, 2002), or for targets at lower frequencies or suspended in water (Tesei et al., 2002; Blonigen and Marston, 2002). Mainly, our experiments show that, by careful selection of ROV tracks and hydrophone chain positions, it is possible to identify individual targets in a multiple-target environment.

The second part of the work presented here was concerned with the localisation of individual scatterers, using multiple-aspect scattering measurements, and the acoustic reconstruction of their shapes. This work showed it was possible to detect these scatterers even in high-noise signals, using an adaptive implementation of the Wiener filters used in seismic data processing. Once processed, these signals can be used for the localisation of the target(s), using multidimensional search routines based on a downhill simplex algorithm. Typical results from the tank experiments are presented, showing the very good agreement between the actual and inferred locations of the targets (as well as their characteristics, in particular for targets of distinct impedances).

These results are important *per se*. Using realistic, scaled targets, proud, half-buried or flush buried, and real seabed types, Section 2 showed it was possible to visually distinguish between close targets, and to some degree detect their different acoustic characteristics (impedance differences, physical structure of the targets, and possibly different reemitted waves). Using the algorithms presented in Section 3, it proved possible to accurately and automatically detect these targets, and quantify the local variations in scattering strengths. It seems quite reasonable that we can now

reconstruct the 3-D structure of multiple-target environments. These results pave the way for multistatic surveys at sea, in environments with multiple targets.

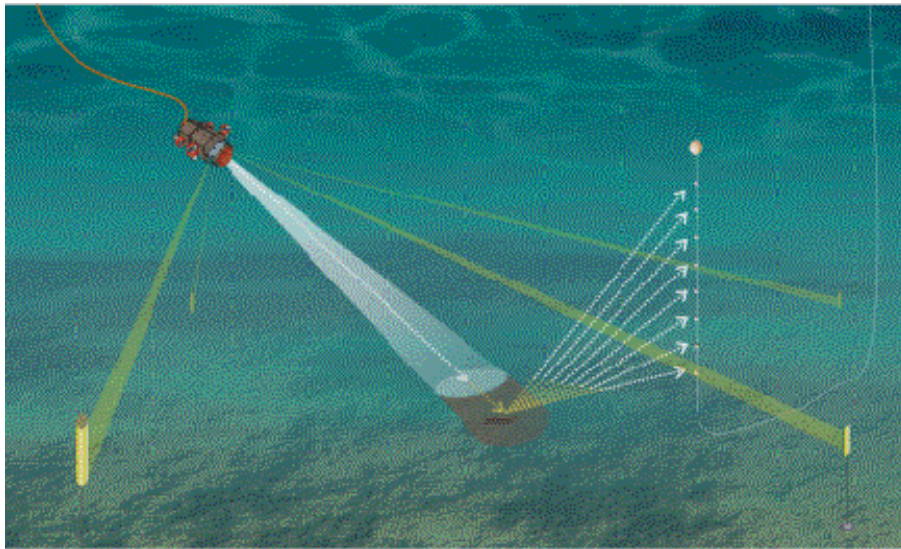


Figure 10. During the SITAR sea trials (late 2003), the ROV was flown above targets of interest, doing both line scans and rotation scans. It was accurately positioned through a transponder net (yellow, upright cylinders in this diagram). The targets were imaged with a narrow-beam parametric sonar, and the scattered signals were received on a hydrophone chain. Preliminary results are consistent with the conclusions from the tank experiments. Image © FOI, Sweden.

The first example was the SITAR sea trials, which took place in the Stockholm Archipelago in September/October 2003. They concentrated on an old ammunition dumpsite, thoroughly documented and ground-truthed (e.g. Caiti et al., 2004; Karasalo and Skogqvist, 2004). One half of the sea trials consisted in testing a parametric synthetic sidescan sonar (Caiti et al., 2004; Zakharia et al., 2004). The other half, aboard HMS Fårösund from the Royal Swedish Navy, consisted in using a Remotely-Operated Vehicle (ROV) with a narrow-beam sonar to image potential targets of interest (Figure 10). Drawing on the lessons learned during the tank experiments, the quality of the raw and processed data were systematically and thoroughly controlled on-board during acquisition. The time synchronisation of the transmitter and receivers proved in particular important. Early analyses showed it was possible to visualise close targets (using the techniques outlined here), despite the occasional failures of some hydrophones. The ROV flew along lines of interest (line scans), and rotated around particular targets (rotation scans). Attitude control proved paramount in getting good localisation of the individual scatterers, as unexpected deviations from the nominal three-dimensional positions had direct repercussions in the localisation process. The processing of the sea trials data is now going on at the different institutions involved and the first results are encouraging. Using the signal processing routines outlined in this article, individual targets can be detected, and it appears that it is possible to accurately reconstruct their exact scattering characteristics, even in multiple-target settings.

Acknowledgments: C. Dyer (University of Bath) is gratefully acknowledged for helping setting up the initial experiments. O. Gómez Sichi provided helpful comments during the internal review of the

manuscript. This work is funded by the European Commission (Framework-V programme SITAR EVK3-2001-00012, coordinated by Prof. A. Caiti, ISME, Italy).

### References

Arya, V.K. and Aggarwal, J.K., *Deconvolution of Seismic Data*, Benchmark Papers in Electrical Engineering and Computer Science, ed. J.B. Thomas. Vol. 24. Hutchinson-Ross (1982)

Blondel, Ph. and B.J. Murton; "Handbook of Seafloor Sonar Imagery", Praxis-Wiley & Sons: Chichester (UK), 314 pp., 1997

Blondel Ph, Pace NG, Heald GJ, and Brothers R. "High-frequency bistatic scattering: modelling and laboratory experiments", in *Proceedings of the Fifth European Conference on Underwater Acoustics ECUA-2000*, p. 869-874, 2000

Blondel, Ph., N.G. Pace, G.J. Heald, R. Brothers; "High-frequency bistatic scattering: comparison of tank and sea experiments", in *Acoustical Oceanography*, T.G. Leighton, G.J. Heald, H.D. Griffiths, G. Griffiths (eds), Proceedings of the Institute of Acoustics, vol. 23(2), p. 276-282, 2001

Blondel, Ph., P. McCloghrie, N.G. Pace, G.J. Heald, R. Brothers; "High-frequency bistatic bottom scattering: Modelling and experimental studies", in *Proceedings of the Sixth European Conference on Underwater Acoustics ECUA-2002*, p. 21-29, Gdansk, Poland, 2002

Blonigen, F.J. and P.L. Marston; "Leaky Helical Flexural Wave Backscattering Contributions from Tilted Cylindrical Shells in Water: Observations and Modeling", *J. Acoust. Soc. Am.*, 112 (2), pp. 528-536, 2002

Bozic, S.M., *Digital and Kalman Filtering*, 2nd ed., Edward Arnold (1994)

Broschat SL and Thorsos EI; "An investigation of the small slope approximation for scattering from rough surfaces. Part II. Numerical studies". *J. Acoust. Soc. Am.*, 1997; **101**(5):2615-2625

Burnett, D.S. and Zampolli, M.; "A unified continuum mechanics approach for structural acoustic finite-element modeling of target scattering", Proceedings of the Seventh European Conference on Underwater Acoustics, Delft (Netherlands), p. 423-430, 2004

Caiti, A., V. Murino, M. Palmese and A. Trucco, Object Reconstruction and Feature Extraction from 3-D Underwater Acoustic Scattering Measurements, In *10<sup>th</sup> International Congress on Sound and Vibration*, Stockholm, A. Nilsson and H. Bodén (eds.), vol. 5, pp. 2449-2456, 2003

Caiti, A., and the SITAR Team; "The SITAR Project – Seafloor Imaging and Toxicity: Assessment of Risk caused by buried waste", Proceedings of the Seventh European Conference on Underwater Acoustics, Delft (Netherlands), p. 757-762, 2004

Canepa, G., N.G. Pace, E. Pouliquen; "Field measurements of bistatic scattering strength of a sandy seabed at 118 kHz", Proceedings of the Sixth European Conference on Underwater Acoustics, Gdansk (Poland), p. 183-188, 2002

Dobbins, P.F., Ph. Blondel, N.G. Pace, I. Karasalo; "SITAR – Localisation and imaging of seafloor targets with multiple-aspect scattering", In *10<sup>th</sup> International Congress on Sound and Vibration*, Stockholm, A. Nilsson and H. Bodén (eds.), vol. 5, pp. 2467-2474, 2003

Dobbins, P.F., N. Jayasundere, Ph. Blondel; "Multiple-Aspect Imaging of Seafloor Targets – Analyses of Tank Experiment Datasets", Proceedings of the Seventh European Conference on Underwater Acoustics – 2004, Delft (Netherlands), p. 469-474, July 2004

Ivanova K and Broschat SL. The method of the local parabolic approximation for rough surface scattering. *J. Acoust. Soc. Am.*, 1993; **94**(4): 2326-2333

Jackson, D.R. A model for bistatic bottom scattering in the frequency range 10-100 kHz. *APL-UW Technical Report TR-9305*, University of Washington, 1993

Jayasundere, N., Ph. Blondel; "Multistatic Imaging of Multiple Targets - Scaled Tank Experiments with a Silt Seabed", (6 pages), CD-ROM Proc. European Conference on Underwater Acoustics – 2004, Delft (Netherlands), July 2004

Karasalo, I., P. Skogqvist; "Transient scattering from submerged and buried objects", (6 pages), Proc. European Conference on Underwater Acoustics – 2004, Delft (Netherlands), p. 451-456, July 2004

- Kirkup SM. *The boundary element method in acoustics*, 1998, Integrated Sound Software Publications
- Kur'yanov BF. The scattering of sound at a rough surface with two types of irregularity. *Soviet Physics – Acoustics*, 1963; **8**(3):252-257
- Lurton, X.; "An introduction to underwater acoustics", PRAXIS-Springer Verlag: Chichester (UK), 380 pp., 2002
- McDaniel ST and Gorman AD. An examination of the composite-roughness model. *J. Acoust. Soc. Am.*, 1983; **73**(5):1476-1486
- Pace, N.G., E. Pouliquen, O. Bergem, A.P. Lyons, *High-Frequency Acoustics in Shallow Water*, NATO Saclant Undersea Research Centre, 612 pp, 1997
- Pouliquen E, Bergem O and Pace NG. Time-evolution modeling of seafloor scatter. I. Concept. *J. Acoust. Soc. Am.*, 1999; **105**(6):3136-3141
- Schenk HA. Helmholtz integral formulation of the sonar equations. *J. Acoust. Soc. Am.*, 1986; **79**(5):1423-1433
- Schmidt H and Glattetre J. A fast field model for three-dimensional wave propagation in stratified environment based on the global matrix method. *J. Acoust. Soc. Am.*, 1985; **78**:2105-2114
- Schmidt H and Kuperman WA. Spectral representation of rough interface reverberation in stratified ocean waveguides. *J. Acoust. Soc. Am.*, 1995; **97**:2199-2209
- Simpson HJ, Houston BH, Frederickson CK and Lim R. Measurements and analysis of scattering from proud and buried targets in a shallow-water laboratory environment, in *Proceedings of the IEEE Conference Oceans'99*, 1999
- Skogqvist, P., I. Karasalo; "A fast acoustic scattering method for buried objects", In *10<sup>th</sup> International Congress on Sound and Vibration*, Stockholm, A. Nilsson and H. Bodén (eds.), vol. 5, pp. 2457-2465, 2003
- Telford, W.M., L.P. Geldart, R.E. Sheriff; "Applied Geophysics – Second Edition", Cambridge University Press, 770 pp., 1990
- Tesei, A., A. Maguer, W.L.J. Fox, R. Lim, H. Schmidt, Measurements and Modeling of Acoustic Scattering from Partially and Completely Buried Spherical Shells, *J. Acoust. Soc. Am.*, 112 (5), pp. 1817-1830, 2002
- Thorsos EI. Exact numerical methods versus the Kirchhoff approximation from rough surface scattering, in *Computational Acoustics, vol. II: Algorithms and Applications*, edited by D. Lee, R.L. Sternberg, M.H. Schultz, p. 209-226, Amsterdam: North-Holland, 1988a
- Thorsos EI. The validity of the Kirchhoff approximation for rough surface scattering using a Gaussian roughness spectrum. *J. Acoust. Soc. Am.*; **83**: 78-92, 1988b
- Thorsos EI and Broschat SL. An investigation of the small slope approximation for scattering from rough surfaces. Part I. Theory. *J. Acoust. Soc. Am.*, 1995; **97**(4):2082-2093
- Voronovich AG. Small-slope approximation in wave scattering by rough surfaces. *Sov. Phys. JETP*, 1985; **62**:65-70
- Williams KL and Jackson DR. A model for bistatic scattering into ocean sediments for frequencies from 10-100 kHz. *APL-UW Technical Report TR-9505*, University of Washington, 1996
- Williams KL and Jackson DR. Bistatic bottom scattering: Model, experiments and model/data comparison. *J. Acoust. Soc. Am.*, 1998; **103**(1):169-181
- Wirgin A. Scattering from hard and soft corrugated surfaces: Iterative corrections to the Kirchhoff approximation through the Extinction Theorem. *J. Acoust. Soc. Am.*, 1989; **85**:670-679
- Zakharia, M., Y. Chevriaux, G. Doignon, J. Dybedal, R. Legallo, C. Pollet; "SITAR prototype, a parametric synthetic sidescan sonar", *Proceedings of the Seventh European Conference on Underwater Acoustics*, Delft (Netherlands), p. 1121-1126, 2004